Experimental Monitoring of Crack Closing and Sliding with Nonlinear Wave Interactions

Alison Malcolm[1], Lauren Hayes[1], Kamal Moravej[1], and Stephen Butt[1]

[1]Memorial University of Newfoundland

November 25, 2022

Abstract

It is now well-established that earthquakes change the seismic velocity of the near surface. There is certainly some understanding of what mechanisms are responsible for these changes, but there remain many questions. Here we attempt to answer the question of the relative importance of different connection mechanisms between cracks and how these change with applied load. To study this, we first perform nonlinear wave-mixing experiments in two sandstone samples at a variety of applied uniaxial stresses. The two samples differ in the relative orientation of their microstructures. We find that although the samples show velocity anisotropy we do not see aligned structures in scanning electron microscope images. By measuring the changes in velocities with applied stress we find that most cracks close during our experiments independent of crack orientation. By contrast, we find that the nonlinear wave interactions vary strongly with applied load and with crack orientation. We analyze these differences and relate them to an emerging model of nonlinear wave interactions with microstructures.

Experimental Monitoring of Crack Closing and Sliding with Nonlinear Wave Interactions

Alison Malcolm [1], Lauren Hayes[1], Kamal Moravej[1], Stephen Butt[2]

[1]Department of Earth Sciences, Memorial University of Newfoundland

[2]Department of Engineering, Memorial University of Newfoundland

Key Points:

- We use experimental observations of nonlinear wave interactions to separate changes in crack opening and sliding as a function of applied load.
- Our experiments support the idea that the nonlinear wave interactions are more sensitive to these crack properties than are linear wave parameters.

Corresponding author: Alison Malcolm, amalcolm@mun.ca

Abstract

It is now well-established that earthquakes change the seismic velocity of the near surface. There is certainly some understanding of what mechanisms are responsible for these changes, but there remain many questions. Here we attempt to answer the question of the relative importance of different connection mechanisms between cracks and how these change with applied load. To study this, we first perform nonlinear wave-mixing experiments in two sandstone samples at a variety of applied uniaxial stresses. The two samples differ in the relative orientation of their microstructures. We find that although the samples show velocity anisotropy we do not see aligned structures in scanning electron microscope images. By measuring the changes in velocities with applied stress we find that most cracks close during our experiments independent of crack orientation. By contrast, we find that the nonlinear wave interactions vary strongly with applied load and with crack orientation. We analyze these differences and relate them to an emerging model of nonlinear wave interactions with microstructures.

1 Introduction

Understanding the nonlinearity in the Earth's response to waves is becoming more important as we try to understand reservoirs in more detail and as we try to understand why and how large earthquakes change the properties of the Earth. For the former, both induced and pre-existing fractures often represent the primary fluid pathway for unconventional reservoirs. Understanding their extent and orientation is thus key to being able to economically exploit these resources. In addition, nonlinearity is becoming a recognized driver of change in more conventional reservoirs (Asaka et al., 2018). At a larger scale, many studies show that the Earth's velocity changes as a result of the passage of large waves from an Earthquake (Wang et al. (2019) give a good recent overview in their introduction). We attempt to simulate this response here using a pump/probe experiment (Renaud et al., 2008, 2011; Gallot et al., 2015) in which we look at the response of a low-amplitude probe wave to the forcing of a large-amplitude pump wave. Here we use a uniaxial load to change the properties of the cracks so that we can better understand how these cracks affect the nonlinear signal. In addition, we present a careful analysis of the fractures present in our sample, and attempt to fit our data to recent theoretical developments by Sens-Schönfelder et al. (2018).

As mentioned above, there are robust observations suggesting that earthquakes change the seismic velocity of the surrounding material (Poupinet et al., 1984; Sato, 1988; Nishimura et al., 2000; Rubinstein et al., 2007; Wegler & Sens-Schönfelder, 2007; Brenguier et al., 2008; Hobiger et al., 2012; Froment et al., 2013; Brenguier et al., 2014; Gassenmeier et al., 2016; Obermann et al., 2019; Wang et al., 2019). There are also strong changes associated with precipitation (Sens-Schönfelder & Wegler, 2006), and volcanic fluids (Brenguier et al., 2014), as well as geothermal production (Hillers et al., 2015; Sánchez-Pastor et al., 2019), and anisotropy changes (Durand et al., 2011). An overview of these applications is given by Sens-Schönfelder and Wegler (2011). Tremblay et al. (2010) look at slow-dynamics (Ten Cate & Shankland, 1996), which is often thought to be the dominant effect in the sorts of post-seismic recovery observed by e.g. Wegler and Sens-Schönfelder (2007); Brenguier et al. (2008) and others. They find that the slow-dynamics effect is more-or-less limited to the source region and does not seem to exist when the receivers are far from the source excitation. That said, there is also evidence that the velocity perturbations are most robust near the stations (see Rubinstein et al. (2007) and references therein), and in the shallow subsurface (Hillers et al., 2015; Hobiger et al., 2016). How to recover the depth of perturbations responsible for observed time delays has also been studied (Obermann et al., 2013, 2014, 2019; Wang et al., 2019). Aoki (2015) gives a concise overview of recent observations and also the theory behind nonlinear elasticity.

The experiments discussed here are of the classical pump/probe type that go back to at least Hughes and Kelly (1953). The most common experiment of this type in the current literature is the Dynamic Acousto-Elastic Testing method (DAET, Renaud et al. (2008, 2012)). In DAET a resonant mode is excited in the sample (the pump) and that mode is then analyzed with a high-frequency probe wave. Rivière et al. (2013) gives a careful experimental overview of this method and the necessary data processing to understand and analyze DAET data and Rivière et al. (2015) carefully compare DAET to the more classical Nonlinear Resonance Ultrasound Spectroscopy (NRUS). Remillieux et al. (2017) provide a large dataset for this method, which is followed up with additional model development to better understand the data in Lott, Payan, et al. (2016); Lott, Remillieux, et al. (2016); Lott et al. (2017). Sens-Schönfelder and Eulenfeld (2019) use Earth tides as a pump and noise as probe in a field experiment analgeous to DAET.

Of particular interest to us is the importance of aligned cracks and their response to applied loads. Aligned cracks are common in the Earth as there are often tectonic forces

that guide crack formation as well as the opening and closing of cracks over time; in-situ rocks are also generally under some form of load (Alkhalifah & Tsvankin, 1995). It remains difficult to definitively separate the response of cracks from other signals, like heterogeneity and intrinsic anisotropy both of the linear elastic moduli and the higher-order moduli. TenCate et al. (2016) give a first attempt at characterizing the importance of the orientation of microstructures relative to the nonlinear wave interactions. A numerical model of these results, given in Rusmanugroho et al. (2020), suggests that what is interpreted by TenCate et al. (2016) as a set of aligned cracks is likely more complicated, with evidence that we should expect almost no nonlinear response when cracks have their normals perpindicular to the particle motion of a P-wave probe. The experiments reported on here aim to separate these signals by running nonlinear elastic experiments repeatedly for a rock under different uniaxial loads. This follows onto work by Zinszner et al. (1997) that looks at classical nonlinear resonance under a variety of loads and saturations and Riviére et al. (2016) who look at DAET under a variety of pressures. Past work points to a decrease in nonlinearity with increasing load and that a pressure of about 10 MPa is enough to more-or-less remove the nonlinear response. Here we go up to roughly 15 MPa and still record a nonlinear response, but our loads are uniaxial whereas past work has looked at confining pressure. Both of these stresses are significantly less than the 40 MPa that Gist (1994) find is required to limit pore-scale flow.

There are a number of theoretical models that can be used to describe the nonlinear response of a rock to either a single strong wave or to the interaction of multiple waves. The introduction of Sens-Schönfelder et al. (2018) gives a thorough recent overview; an overview of earlier work is given by Ostrovsky and Johnson (2001) and an overview of work relating to cracks is given in Broda et al. (2014); the entire field of nonlinear elasticity is covered in the recent book by Guyer and Johnson (2009). All of these models build upon the original so-called five constant model (Landau & Lifshitz, 1970), which describes a second-order dependence of stress on strain by adding an additional three cubic moduli (usually called A, B, C) along with the usual two second-order elastic moduli (e.g. the Lamé parameters λ, μ). This model describes so-called classical nonlinearity where the material responds to strain in a nonlinear way, but without the stress/strain hysteresis, end-point memory, or slow-dynamics present in Earth materials (Guyer & Johnson, 2009). Building upon this model, McCall and Guyer (1994); McCall (1994) describe P-M space, which incorporates hysteresis as a way of accounting for the difference in the

response of a crack (or other hysteretic element) during its opening and closing phases. Nazarov et al. (1997) gives an early discussion of how both linear and nonlinear elastic constants change in cracked media, looking only at crack opening and closing, but not allowing for sliding. Lebedev and Ostrovsky (2014) take into account forces between grains and the adhesion forces between grains and look at how these two forces balance one another and lead to nonlinear effects. Scalerandi et al. (2015) build on the PM space model to derive the expected behaviour of harmonics for different mechanisms and then give experimental data to illustrate how the power in these harmonics changes with increasing damage in a sample. Solodov et al. (2002) explicitly study clapping cracks (i.e. when the faces touch). More specifically they explain how a closed crack responds to stress as compared with an open crack. Zhao, Qiu, and Jacobs (2016); Zhao, Qiu, Jacobs, and Qu (2016) follow-up on this work, generalizing it to allow for sliding, but keeping the difference between the response of open and closed cracks. Zaitsev et al. (2014) develop a model based on thermal fluctuations at the nano-scale. Vakhnenko et al. (2006) develop a soft-ratcheting model that describes several nonlinear phenomena. Norris (2007) explains how to develop a model via the packing of spherical grains and the changes in the deformation of these grains. He then uses this model to explain differences in the nonlinearity of perfect sphere packs and rocks. From other fields, in particular biomechanics, we can also gain insight. For example in Bose and Dorfmann (2009), they add a strain-dependent term to the strain energy functional and find that this adequately models the hysteresis in muscle response in caterpillars during muscle firing and relaxation. For this paper, we focus most on the model of Sens-Schönfelder, Snieder and Li (Snieder et al., 2016; Li et al., 2018; Sens-Schönfelder et al., 2018), henceforth the SSL model. We choose this model because it is straightforward to implement and splits the nonlinear response into a number of elements describing different types of perturbations to cracks. Specifically, in Snieder et al. (2016), they develop a model that describes the breaking and healing of connections across cracks. Their model is a straightforward ordinary differential equation describing the evolution of a set of pillars with which they model cracks as a function of time. They enhance their model in Sens-Schönfelder et al. (2018) by incorporating several additional mechanisms including shearing on the crack and a straightforward stress dependence of the modulus. In this paper, we use this splitting of the strain to better understand our experimental results.

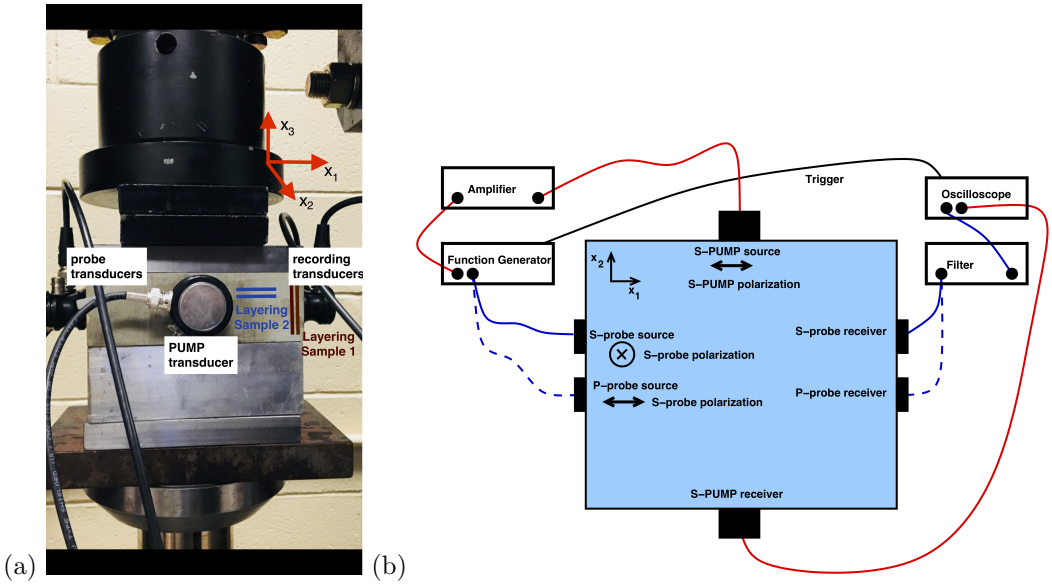

Figure 1. This figure illustrates the experimental setup within the press, and sets up the coordinate system to be used later. The stress is applied only in the x_3-direction. (a) A picture of the entire experiment. (b) Schematic of the experimental setup.

The paper is organized as follows. We begin by describing our experimental setup and showing our experimental data. Next we analyze scanning-electron microscope (SEM) images of our samples to look for aligned structures. Following this, we measure the velocity changes as a function of uniaxial load and use the model of Browning et al. (2017) to estimate the perturbations to the cracks in the sample caused by the loading. Next we fit our results to the model proposed by Sens-Schönfelder et al. (2018) and use that model to interpret what is changing at different loads. We combine these results to summarize the improvement in our understanding of how the parameters of cracks effect the nonlinear interaction of different waves.

2 Experimental Setup

Our basic experimental setup follows that described in Gallot et al. (2015); Ten-Cate et al. (2016), and is shown in Figure 1. The basic goal of our experiments is to directly follow the propagation of a strong pump using a weaker probe wave as a sensor. We do this by sending two waves into a sample: A large-amplitude, low-frequency (90 kHz) pump wave, and a smaller-amplitude, higher-frequency (1 MHz) probe wave. To ensure that the probe is indeed weak, we use a signal that is roughly two orders-of-magnitude

weaker in strain for the probe (strain of about 10^{-8}) than for the pump (strain of about 10^{-6}). Using the coordinate system defined in Figure 1, the pump transducer is placed on the positive x_2-face with polarization along the x_1-axis, roughly through the centre of the sample. We explore two probe signals, one P-wave propagating and polarized along the x_1 direction and an S-wave probe propagating along the x_1 direction with polarization in the x_3-direction. The idea is that the pump perturbs the sample, likely by dynamically changing the crack properties, resulting in a change in the probe velocity. The change in the probe velocity will result in a traveltime change in the probe signal. We record all signals on the positive x_1-face using transducers identical to those used to excite the probe. All transducers are Olympus videoscan transducers; the pump transducer has a resonance frequency of 50 kHz and the probe transducers have a resonance frequency of 1 MHz. The pump transducer is driven at a frequency of 90 kHz and runs for four cycles, and the probe transducers at a frequency of 1 MHz and are run for a single cycle. These frequencies are chosen to generate clear signals that look as similar as possible to the input signals. All signals are generated with a standard function generator and recorded with a standard oscilloscope. The pump signals are amplified with an E & I 240L RF power amplifier and all recorded signals are high-pass filtered with a Krohn-Hite adjustable digital filter with cut-off frequency of 600 kHz. We wrapped the sample in plastic wrap to diminish the influence of humidity changes on the results. The sample was otherwise kept at room conditions, in an interior climate-controlled room. We would certainly expect to see changes in that environment over the course of the experiments, and the local humidity over the period of the experiment averaged 83% with significant excursions to a high of 100% and low of approximately 40%, with all days averaging between 75 and 95%.

We repeat our experiments at several different uniaxial loads applied using a hydraulic press. The sample is placed in the cell betweeen two stainless steel plates to uniformly distribute the load on the sample. Several spacers are needed to place the sample in contact with the pistons of the press.

We study two different samples of Crab Orchard Sandstone with different orientations of layering, which are shown in Figure 1. (Benson et al., 2005) studied this particular rock and conlcuded that it has an aligned pore-space. For each sample and each applied load, we perform two experiments: one with the P-wave probe and one with the S-wave probe. In Figure 2, we plot our experimental results. These plots are described

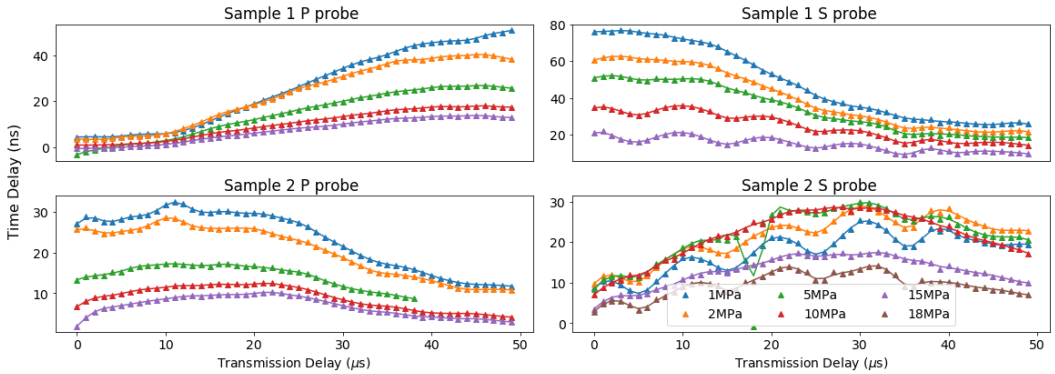

Figure 2. Time delay data for both samples at a variety of applied loads.

in detail in Gallot et al. (2015), so we give only a brief description here. Each data point on each curve is calculated from three recorded signals: S_1, the probe by itself, S_2, the pump and probe together and S_3 the pump alone. We then calculate $S_2 - S_3$ to obtain a perturbed probe signal. The traveltime delay is the difference in the arrival time between the original probe (in S_1) and perturbed probe (in $S_2 - S_3$). We compute this traveltime delay by fitting a sinc function to the five points nearest the peak of the cross-correlation of the two signals. This follows the suggestion of e.g. Catheline et al. (1999), replacing the parabola with a sinc function because in fitting the peak we are essentially assuming that we have undersampled our signals, for which a sinc interpolation is the optimal solution (Gholami, 2018). We then change the transmission delay time between the pump and probe and measure the same three signals to obtain the next data point. The data collection takes about one hour for a single applied stress and pump/probe combination. For each sample and pressure we collect two datasets, one with the probe a P-wave and the other with the probe an S-wave. All data use an S-wave pump. Hayes and Malcolm (2017) find that the relative polarizations of the two S-waves are not particularly important.

3 Experimental Results

Note that a preliminary version of these data, along with preliminary interpretations were given in Hayes et al. (2018). Figure 2 shows the data recorded for both probe types and both samples. We see a clear decrease in the maximum amplitude of the traveltime delays as a function of applied load for all experiments except for the S-probe in

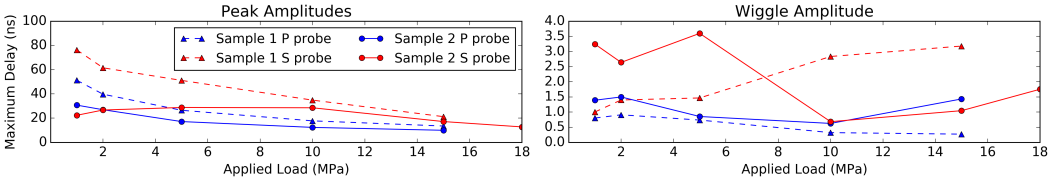

Figure 3. Combining all of the data onto a single plot, we see that the trend for amplitudes is clear; the overall amplitudes (left) decrease, whereas for the higher-frequency wiggles (right) there is no clear trend over all samples.

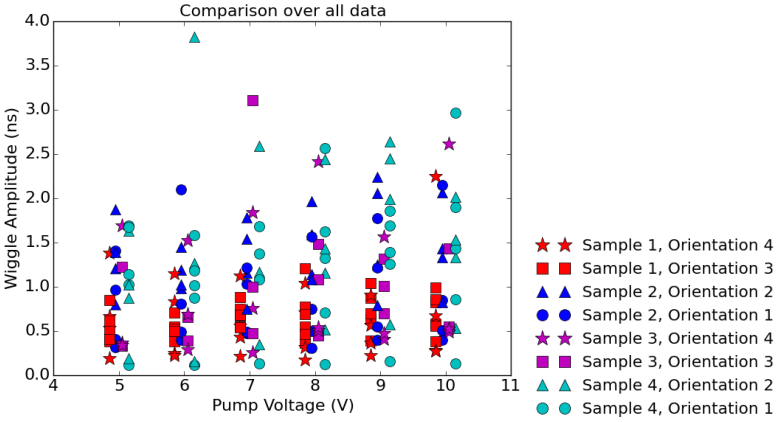

Figure 4. The dependence of the high-frequency part of the signal on the driving voltage of the pump. The different symbols refer to different samples and relative orientations of the cracks and the probe. Data are shown from four different samples of the same Crab Orchard Sandstone used for the other experiments. Note that there is no increasing trend as we increase the magnitude of the pump forcing.

Sample 2. In addition, and as reported previously (Gallot et al., 2015; TenCate et al., 2016), we see two clear frequencies in the signals. The first is at roughly the period of the input pump signal and the second roughly follows the envelope of the pump signal. The latter is what results in some pump/probe combinations showing an increase in time delay with transmission delay while others show a decrease (compare Figure 2(a) and (b)). Whether we sense the increasing part of the pump signal envelope or the decreasing part depends on which part of the pump signal is seen by the probe and is largely due to the geometry of the samples and the precise relative locations of the pump and probe transducers. Thus in (a) we are seeing the beginning of the pump signal, starting from before the pump and probe begin to interact whereas in (b) we are looking at the end of the pump signal beginning from where it has its maximum amplitude and ending somewhat after the pump signal has passed through the pump/probe interaction region in the center of the sample. It is this low-frequency part of the signal that (TenCate et al., 2016) found to change with sample orienation.

In Figure 3, we isolate the changes in the signals as a function of applied load. Figure 3(a) shows the maxima of each dataset. To compute this, we simply take the maximum value of each dataset and plot it as a function of applied load for each dataset. This clarifies our observation above that we see a monotonic decrease in the traveltime delays as we increase the applied load, except for Sample 2 with an S-probe. An S-wave probe senses changes in the shear modulus (assuming the density doesn't change). So this seems to indicate that low applied loads in Sample 2 make it easier to perturb the shear modulus, following which it becomes more difficult to make these perturbations as the load is increased.

To compute the amplitude of the higher-frequency component, we first filter the data with a butterworth bandpass filter with corner frequencies 50 and 150 kHz and then take the maximum of the filtered signal. We see that the amplitude of the total signal decreases significantly with increased stress whereas the amplitude of the high-frequency part of the signal is more-or-less independent of the applied stress. This is similar to other data that have shown the amplitude of this high-frequency part to be independent of sample orientation (TenCate et al., 2016). In fact, we find that this signal is even independent of the driving voltage of the pump. This is shown in Figure 4, where we plot the amplitude of this signal over a few dozen experiments taken over several months on a total of four samples of the Crab Orchard Sandstone used here (including our two sam-

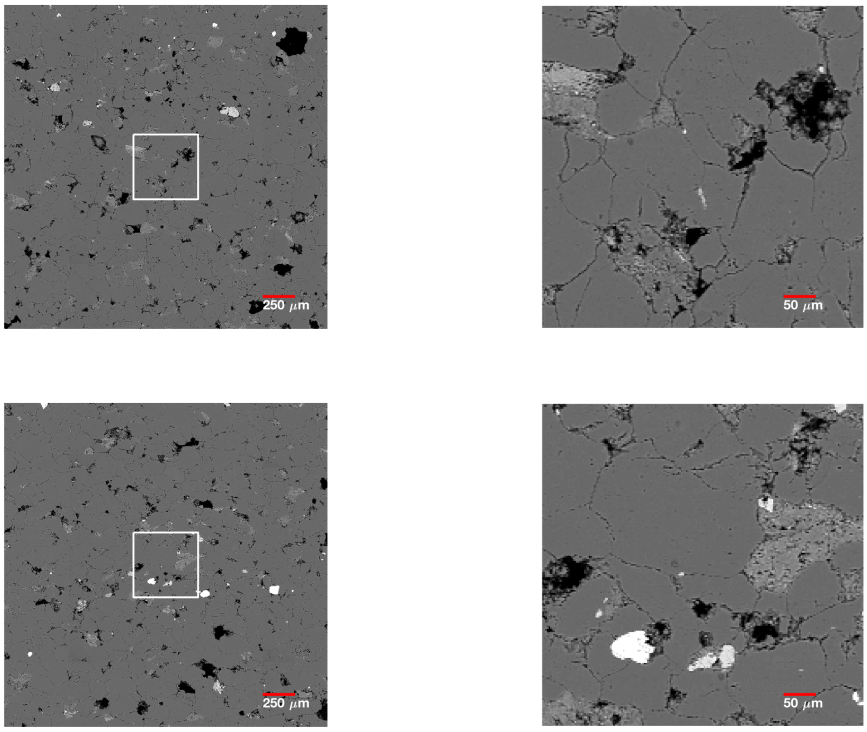

Figure 5. SEM images of the sample 1 (top) and sample 2 (bottom). The black box is shown zoomed in beside each image.

ples before any load was applied to them). These four samples have two different orientations of bedding and are each measured in two different orientations (the samples are described in more detail in TenCate et al. (2016)). What controls the signal at this frequency remains an open question.

4 Estimating Crack Orientations

To obtain ground-truth measurements on the crack orientations in our samples, we generated thin sections of each sample, which we then image in a scanning-electron microscope (SEM). These two thin sections were cut so that they provide two cross-sections of the structure, one parallel to the layering (Sample 1) and one perpendicular (Sample 2). We show subsets of these images at two scales in Figure 5. We show 1000 by 1000 pixel images. In total we process 6000 (6000) by 10,000 (12,000) pixels in Sample 1 (2), determined by the biggest rectangle that would fit within the scanned area. Following Arena et al. (2014), we first generate a black and white version of our SEM images. We

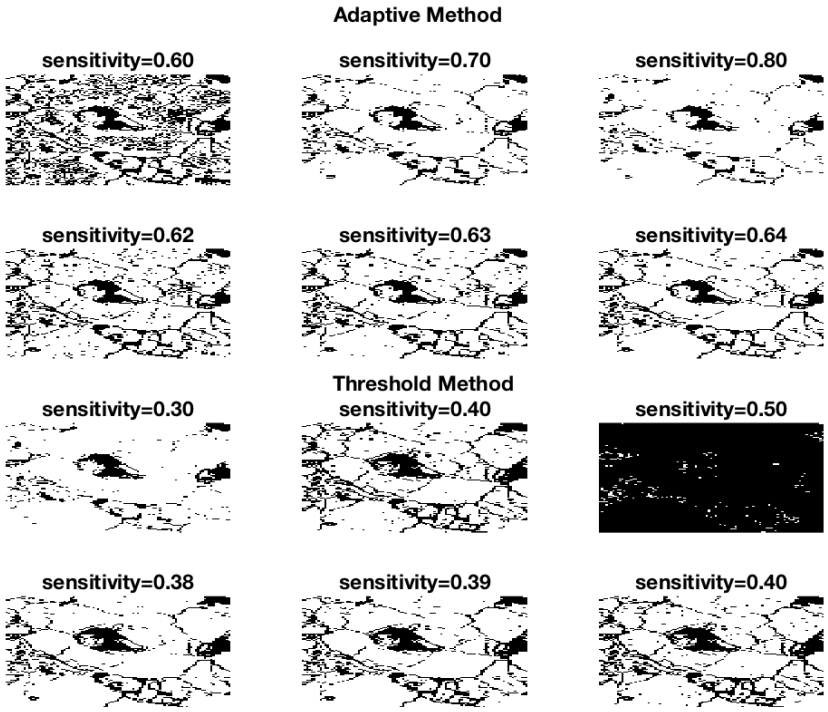

Figure 6. Illustration of the conversion of the SEM images to black and white. We chose the threshold method with sensitivity of 0.39, but as can been seen in the figure changing this somewhat does not strongly impact the results.

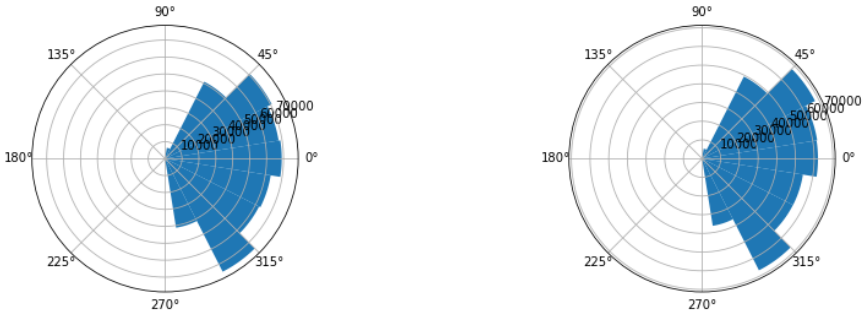

Figure 7. Rose diagrams for fracture orientation for Sample 3 (left) and Sample 4 (right). These data are based on roughly 500,000 cracks per sample and show no evidence of a preferred fracture orientation.

do this with a simple threshold and the imbinarize function from Matlab. We use a simple threshold of 0.39 because this gives visually better results that Otsu's method or the adaptive method provided in Matlab. This is illustrated in Figure 6. We then process the black-and-white images to determine fracture orientations. To do this, we first find all pixels that are black as these are the pixels that are empty so to speak, generating a list of zero pixels. We then remove the pores, by removing all pixels that are surrounded by zero pixels. Following this we tie together pixels that are touching (i.e. hold together to form a linear feature of some sort). This essentially splits our set of black pixels into a list of connected pixels, which we call cracks. We then remove cracks that contain less than three points (changing this to ten has little effect), and cracks that have more than two points in common. Finally, we fit each remaining crack to a line and extract the angle from horizontal of that line, which is plotted in the rose diagram in Figure 7. Although there are certainly other ways of estimating fracture orientation, we don't expect a large change in the final conclusion by varying this.

For each image, we process the image in 500 by 500 pixel chunks to save memory. Although this may count some fractures twice as they span the boundary of a region, we processed roughly 500,000 cracks for each image so the sample size is likely to still be statistically significant. In the images in Figure 5, we do not see evidence of aligned structures, but rather cracks that appear to surround the grains in the samples. This is confirmed by the rose diagrams in Figure 7, which show the crack density as a function of crack orientation. A plausible remaining explanation for why we see differences in crack response as a function of direction is that cracks in different directions have different compliances. We attempted to determine whether some cracks were thicker than others but our SEM images do not have sufficient resolution to determine this. Another possible explanation for the results seen previously with these samples, and our own results, is that it is not the cracks themselves but rather the interface between the different visible layers in the samples that cause our observed differences. This is interesting as it seems that at the micro-scale our samples have relatively homogenous structures, but they still show velocity anisotropy and an orientation dependence of the nonlinear response (e.g. the difference in maximum delay time between Sample 1 and 2 with the S-probe). Because we do not see a variation in cracks, we refer to the orientation of layering, rather than cracks.

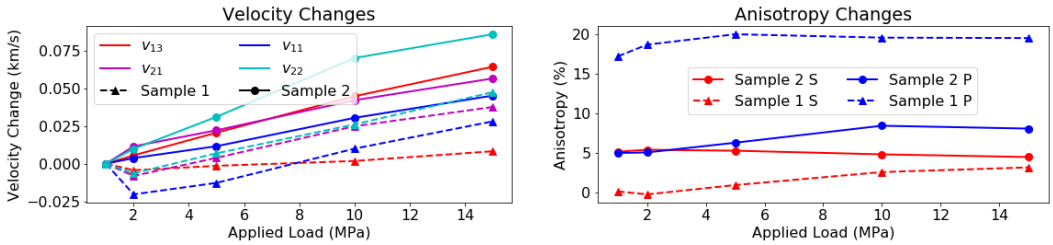

Figure 8. (a) All of the velocities measured increase as a function of applied stress. Note the slight decrease in the velocities of Sample 1 at low pressures, and the anomolous behaviour of v_{13} for Sample 1. (b) The anisotropy is most significant for P-waves in Sample 1 as expected when looking at the geometry shown in Figure 1. Note that the anisotropies are calculated using the velocities in (a) so the P-wave anisotropy is between the 1- and 2-directions whereas the S-wave anisotropy is between the 13 and 12 directions. There is no significant change in anisotropy with applied stress.

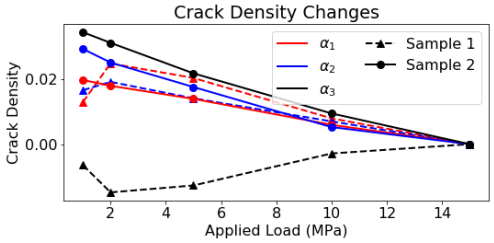

Figure 9. Recovered changes in crack density, in general the crack density decreases with applied load, indicating crack closure. The exception is α_3 for Sample 1 which increases.

5 Estimating Crack Closing

Having established that our samples contain cracks in all orientations, in this section, we follow the work of Browning et al. (2017) to estimate the proportion of the cracks that have been opened or closed during the experiment. Using their notation, re-iterated in Figure 1, we are able to measure four velocities: v_{11} (P-probe), v_{13} (S-probe), v_{21} (S-pump), and v_{22} (P-wave generated by S-pump). Note that while all data used to make the plots in Figures 2 are measured on the probe transducer on the positive x_1-face, we also record the pump signal on the pump transducer on the negative x_2-face, which is where we obtain v_{22} and v_{21}. To measure the velocities shown in Figure 8, we first pick the traveltimes. For the lowest pressure (1 MPa), this is done by picking the zero-crossing before the peak within a user-defined time window. Each pick is then manually checked

Table 1. Dimensions and velocities (at 1 MPa) for each sample.

	x_1 (mm)	x_2 (mm)	x_3 (mm)	v_{11} (mm/μs)	v_{13} (mm/μs)	v_{21} (mm/μs)	v_{22} (mm/μs)
Sample 1	155	126	52	2.48	1.81	1.80	2.39
Sample 2	154	125	52	2.17	1.78	1.80	2.26

to ensure that it chose the correct arrival. For higher pressures, we measure the traveltime change by cross-correlating the waveforms with those recorded at 1 MPa. When we are extracting the P-wave velocity from measurements of the S-wave pump, the P-wave is much smaller than the S-wave and so to recover a reliable velocity change we window the data roughly to include only the P-wave. We do not need to window when measuring the S-wave traveltime because the S-wave is much stronger. For measurements on the probe signals, we record only about 2 periods of the signal and so there is no interference between different wavetypes. We measure the dimensions of the samples with calipers and use them to convert the traveltimes to velocities; these values are given in Table 1. We use the repeated measurements on the pump signals (for the two probes) to estimate the errors in our recovered velocities at less than 5%. The velocity changes are shown in Figure 8. In this figure, we see that as expected, the anisotropy is significantly larger for the P-waves in Sample 1; in this sample the P-wave probe (v_{11}) travels across the layering (the slow direction), whereas the P-wave excited by the probe travels along the layers as do both P-waves in Sample 2 (the fast direction). All of the anisotropies increase slightly and then plateau or decrease at higher applied stresses. This seems to indicate that the applied load first opens some cracks (increasing anisotropy) and then closes them (decreasing anisotropy).

Following Browning et al. (2017), equations (14-19), and section 1.3 of Tsvankin (2012), we are able to recover the stiffness coefficients, C_{IJ} (using Voigt notation, Nye et al. (1985, p. 135))

$$\begin{aligned} C_{11} &= \rho v_{11}^2 \\ C_{22} &= \rho v_{22}^2 \\ C_{55} &= \rho v_{31}^2 \end{aligned}$$

$$C_{66} \quad = \quad \rho v_{12}^2 \,, \tag{1}$$

where ρ is the density, as a function of applied load. Now we use that $S^{-1} = C$ to estimate the compliances, and we take the values of S in terms of elastic parameters assuming a orthorhomic material (i.e. two sets of fractures). Recalling the scaling (Nye et al., 1985, p. 134) of the elements of S_{ij} the elements of s_{ijkl} are

$$\begin{aligned}
s_{1111} &= S_{11} &&= \frac{v_{11}^2 - v_{13}^2}{\rho v_{13}^2 (3v_{11}^2 - 4v_{13}^2)} \\
s_{2222} &= S_{22} &&= \frac{v_{22}^2 - v_{21}^2}{\rho v_{21}^2 (3v_{22}^2 - 4v_{21}^2)} \\
4s_{1313} &= S_{55} &&= \frac{1}{C_{55}} = \frac{1}{\rho v_{13}^2} \\
4s_{1212} &= S_{66} &&= \frac{1}{C_{66}} = \frac{1}{\rho v_{21}^2}
\end{aligned} \tag{2}$$

where the last equalities come from the definition of S_{IJ} (Boresi & Schmidt, 2003, equation 3.51), and the complicated expressions for S_{11} and S_{22} are the inverse of Young's Modulus in the 1- and 2-directions written in terms of the velocities.

Using the expressions in Equation 2, we estimate the compliances as a function of the applied uniaxial stress. Continuing to follow Browning et al. (2017), who build on Sayers and Kachanov (1995) and (Guéguen & Kachanov, 2012), we estimate the change in crack density as a function of this stress in all three directions, α_j, $j = 1, 2, 3$, where α_j is the crack-density for cracks with normal in the j-direction. To do this, we require both the compliance at different stresses and the compliance of the un-cracked matrix. Since we do not have the latter quantity, we approximate it with the compliance at the highest stress. This assumes that all of the fractures in the sample are closed at this stress, which is almost certainly not the case. This means that the crack densities we obtain at different pressures are not absolute crack densities, but densities measured relative to the density at the highest stress. There are six expressions in total for these α_j parameters, but because we are able to measure only four velocities, as discussed above, we estimate

$$\begin{aligned}
\Delta S_{11} &= h\alpha_1 \\
\Delta S_{22} &= h\alpha_2 \\
\Delta S_{44} &= h(\alpha_1 + \alpha_3) \\
\Delta S_{55} &= h(\alpha_1 + \alpha_2) \,,
\end{aligned} \tag{3}$$

where $h = 32\frac{1-\nu^2}{3E(2-\nu)}$, E is Young's Modulus and ν is Poisson's Ratio; we use the average values of these parameters over the x_1 and x_2 directions. The results of estimating these α's for both samples are shown in Figure 9. We use the fourth equation in 3 to estimate the error in our estimates of the α_j's, because we can estimate α_1 and α_2 from the first two equations, we can compare their sum to the fourth equation. This gives a rough estimate of our error to be 35% for Sample 1 and 10% for Sample 2.

The results in Figure 9 show relatively small crack densities (1/10 of those in Browning et al. (2017), though it is not clear what they used as a reference state). In addition, we see that we are closing cracks in all directions except the 3-direction in Sample 1. (Note that increasing α indicates an increase in crack density, which can be interpreted as either generating new cracks or opening existing ones.) In Sample 2 and the 1- and 2-directions of Sample 1, this indicates that the applied stress is closing cracks. In Sample 1, this appears to start between 2 and 5 MPa, whereas for Sample 2 we seem to start closing cracks at 1 MPa. This is somewhat counter-intuitive as we would expect cracks with normals in direction 1 and 2 to open under a load on the 3-axis. A possible explanation is that the cracks are not perfectly aligned with the layering in the sample; in fact we know that we have cracks in almost all directions from the SEM analysis above. Thus we could be closing the cracks that are aligned with the stress even when the layering is perpindicular to the stress. Another possible explanation is that we may in fact be introducing shearing rather than opening or closing. If we follow the model of Borri-Brunetto et al. (2001); Sens-Schönfelder et al. (2018) we can explain the results for α_3 in Sample 1. In their model, they assume that the two sides of the crack fit together in the ambient state, and then slide against each other eventually becoming uncorrelated. This could be what is happening here, at low stress we first shear the crack slightly, decreasing the crack density as the two sides of the crack align. As the stress is increased, the two sides continue to slide resulting in poorer contact and thus more open cracks and higher crack density. The reason this happens only for α_3 of Sample 1 is likely due to the alignment of the layers with the load. In this sample, the layers are aligned with the applied load, so we would expect cracks aligned with these layers to open or slide.

6 Comparison with Snieder-Sens-Schönfelder Model

In this section we attempt to fit our data to the phenomenological model of Snieder et al. (2016); Sens-Schönfelder et al. (2018), which we will call the SSL model. In addition to a background modulus, their model has three parts:

1. A decrease in modulus with strain, which we will call "the strain mechanism" in what follows, modeled via
$$\Delta M_1(t) = -A\epsilon(t)\,, \tag{4}$$
where ϵ is the applied strain.
2. Shear motion on a crack, which assumes that each crack has a roughness that is correlated but not aligned across the crack, following Borri-Brunetto et al. (2001) as described at the end of the previous section. In equilibrium the two faces of the crack fit together for a maximum modulus, as the crack is sheared the two faces move apart and are thus less correlated, decreasing the modulus. As more strain is applied, the two sides move far enough that they are no longer correlated, and thus the modulus no longer depends on the applied strain. We will call this "the shear mechanism". They model this with a Gaussian
$$\Delta M_c(t) = B\left(\exp\left[\frac{-\epsilon(t)^2}{2w^2}\right] - 1\right)\,, \tag{5}$$
where w is the width of the Gaussian.
3. Frictional interfaces, or broken connections, that open or close with applied stress, which we will call "the connections mechanism". They propose a model in which the modulus changes with the number of connections between these pillars, $N(t)$
$$\Delta M_s(t) = -CN(t)\,. \tag{6}$$
The number of broken connections is found via
$$\frac{dN_i}{dt} = \frac{\nu|\dot{\epsilon}|}{\tau_i}(1 - N_i) - \frac{1}{\tau_i}N_i\,, \tag{7}$$
in which $\dot{\epsilon}$ is the strain-rate. If the number of connections $N_i = 0$ then all possible connections of type i are closed and $N_i = 1$ indicates that all of this type of connection is open. The relaxation time, τ_i controls how quickly connections of type i form and break. To estimate the total number of connections we then sum the contributions over i. We do this by setting up a log distribution of τ_i between t_1 the shortest relaxation time and t_2 the longest relaxation time. Because

we sample a log distribution, rather than a linear distribution we sum

$$N = \frac{1}{n_\tau} \sum_i N_i \,, \tag{8}$$

where n_τ is the number of time-scales used. Because we use this log distribution of relaxation times, this equation is slightly different that the corresponding summation in Sens-Schönfelder et al. (2018, eq. 6).

Taken together the modulus as a function of time is then

$$M = M_0 + \Delta M_l + \Delta M_c + \Delta M_s \,. \tag{9}$$

To fit our data to this model, we must make several approximations. First, the model depends on the strain, which we do not measure directly. We do measure the pump signal on a transducer opposite the transducer that generates it (see Figure 1), from which we can roughly estimate at least the time-dependence of the strain. We do this by first shifting the time axis to estimate the signal that would have been at the location of the pump/probe interaction, and then scaling the transducer signal to a maximum amplitude of 10^{-6}. We scale the data because the transducer measures a voltage not a strain. In similar experiments we measure a strain amplitude of roughly 10^{-6}, which is why we choose to scale to this value. The amplitude of this signal does not change with applied load, so we assume that there is no change in the strain amplitude with applied load. This does not give us a precise value of strain, and thus the absolute values of our fit parameters should not be interpreted, but this does not hinder the interpretation of the relative magnitude of these parameters. The second approximation pertains to where and when the signals interact. To estimate this carefully would require extensive modeling of the experiment, but we can get a reasonable estimate by assuming the waves travel a straight path across the sample and then shifting the signals in time back to the time when they would have been at the interaction point where the pump and probe signals cross. To estimate this, we calculate the time it would take the probe wave to arrive at the center of the sample (aligned with the pump transducer) and shift the transmission delay forward by that amount of time. In Figure 10, we compare the shifted normalized pump strain to the shifted normalized delay times. We do not take into account the changing velocities with applied load because these changes shift the data by significantly less than a wavelength. We see that shape of the two delay curves agree reasonably well with the shifted strain indicating that we have aligned the signals appropriately. Our third

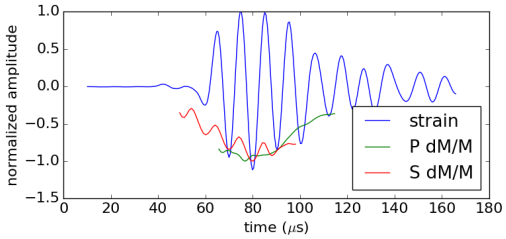

Figure 10. To check that our estimated delays align with the shape of the applied strain, we plot them together here. Note that we are plotting shifts and not delays, which is why the y-axis appears flipped as compared with previous plots.

approximation is that the SSL model estimates the perturbations in modulus, whereas we have been measuring the perturbation in traveltime. Because $M = \rho v^2$ the two are easily related via

$$\frac{dM}{M} = \frac{2\rho v dv}{M} = \frac{2dv}{v} = 2\frac{dT}{T}\,, \tag{10}$$

allowing us to easily translate our changes in traveltime to changes in modulus. Since the scaling is so simple, errors in the estimate of the total traveltime will not effect the fit any differently than the scaling of the strain. As a final approximation, several of the parameters in this model fit the strain-rate or strain squared, both of which have dominant frequencies at twice the frequency of the applied strain. We do not see this signal in our data and so we filter the strain with a low-pass filter with corner frequency of 150 kHz to remove the double-frequency signal (which we expect at approximately 180 kHz), while keeping the signal at the strain frequency (90 kHz). In summary, we are able to process our data to fit this model, but in order to do so we lose the ability to fit the absolute amplitude of the coefficients A, B, C. We can still reasonably expect to recover their relative importances as well as the parameters $w, \tau_{\min}, \tau_{\max}$.

We fit our data to this model using a standard nonlinear least-squares data fitting algorithm (`curve_fit` in python). The model involves seven parameters $(A, B, C, \nu, w, \tau_{\min}, \tau_{\max})$, which makes it difficult to fit them all simultaneously. Thus we explore how well our data constrain each of the parameters before deciding which to fit, what initial values to use, and what bounds to put on each parameter. We do this using a subset of the data that seem to represent most of the qualities we see in the entire data set, specifically we use data from both samples at 15 MPa because they show some oscillations at the pump frequency as well as including data that cover both increasing and decreasing modulus changes.

In addition, we fit the Sample 2 data at 1 MPa because these data have additional oscillations at the pump frequency. The results of this are shown in Figures 11 and 12, and the parameters of the various inversions are given in Table 2.

We first fit each part of the model separately, setting the rest of the model to zero. We do this to see whether our data can be explained adequately with only a subset of the mechanisms in the SSL model. Looking at the results in Figure 11, we see that we can fit the data reasonably well with either the shear (inversion 1B, in which $A = C = 0$) or connections mechanisms (1C, in which $A = B = 0$), but the strain mechanism is not able to fit most of the datasets (1A, in which $B = C = 0$). This seems to indicate that most of our signal is coming from the cracks in the rock rather than its intrinsic nonlinearity, which one might expect to be proportional to the strain. To refine these fits, we use the recovered parameters from each of the individual inversions (1A, 1B, 1C), to refine the parameters for each mechanism separately (inversions 2). The results are quite similar in that we cannot fit the data adequately by refining on the A parameter even when fixing the other parameters to reasonable values. From these inversions we note that $(\tau_{\min}, \tau_{\max}, \nu)$ change little throughout the various inversions. We thus fix these parameters to (-8,-2,0.8), and invert for the other four (A, B, C, w) together in inversion 3. Our values of $\tau_{\min}, \tau_{\max}$ are smaller than those in Sens-Schönfelder et al. (2018) by between 3 and 4 orders of magnitude. The parameters that we use make sense given our frequency and their suggestion that $\tau_{\min} < 1/f < \tau_{\max}$; for us $1/f = 2 \times 10^{-5}$ which is right in the centre of our chosen range (10^{-8}–10^{-2}). We next take the results of inversion 3 as initial values and re-run the process fitting all parameters at once. This does not update any of the parameters significantly (compare black and green symbols in Figure 12) and the errors in the data fit remain approximately the same. This inversion is not shown in Figure 11 as the lines are directly on top of the fits for inversion 3. When fitting all of the data, we noticed a trade-off between B and w, we thus fit only A, B, C in inversion 5. This also does not change the visual quality of the fit significantly and so we do not show it in Figure 11. We thus conclude that the strategy used in inversions 3 or 5 is the best of those studied as it is more computationally efficient than fitting all of the parameters simultaneously, but gives similar results. As a final note on inversion strategies, we find that the fitting process is not particularly sensitive to the initial values of A, B, C, w, ν, but is quite sensitive to the initial values of $\tau_{\min}, \tau_{\max}$ and does not generally adjust these values or those of ν during the inversion. In addition, when fit-

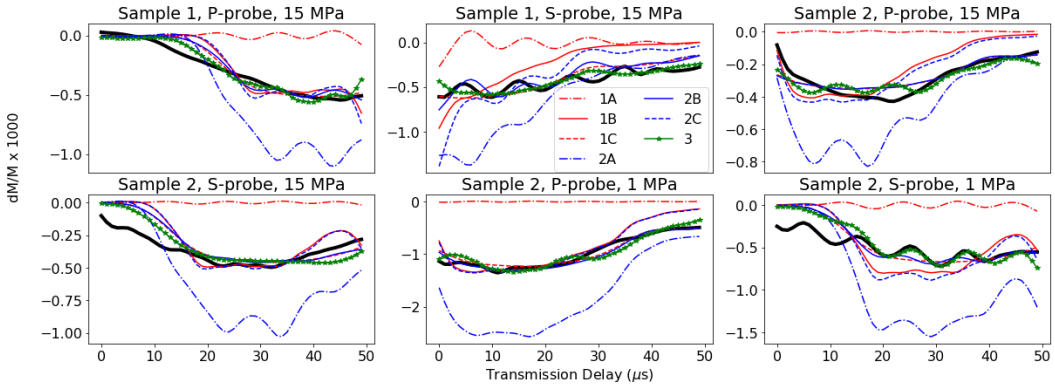

Figure 11. This figure compares the results of three of the different inversions run on the data (the results of inversion 4 and 5 overlay those of inversion 3 and so are not shown). The parameters for the various inversions are shown in Table 2. The title of each plot gives the dataset fit. Note that the vertical scale is multiplied by 1000 for display purposes. Most datasets can be fit reasonably well with either of the shear or connection mechanisms. The thick black line is the data.

ting all of the data we will find that there is a significant trade-off between B and w. From this experience, it seems quite likely that there are a lot of local minima in our intrinsic objective function. We comment further on which parameters are robustly recovered at the end of this section.

Having settled on an inversion strategy, we now fit all of the recorded data and present the results in Figure 13. There are a few noteworthy trends. First, the data are generally fit better during the part of the experiment where the modulus is increasing back to zero than when it is decreasing (note the mis-match at early transmission delays for Sample 2 with the S-probe and Sample 1 with the P-probe). It is difficult to say why this might be. One speculation is that the model is less accurate for low strains, another is that the data alignment may be more important at these lower strains, yet another is that the model is designed with relaxation in mind more than initiation of change. Second, although we are well able to fit the oscillations in the Sample 2 S probe data, we are less successful in fitting these oscillations in other datasets, and often the oscillations are present in the fit, but not the data (as can be seen in the residuals in Figure 14 many of which have oscillations. The model clearly does a good job of fitting the trend of the data with applied load. When looking at the residuals it is also clear that for Sample

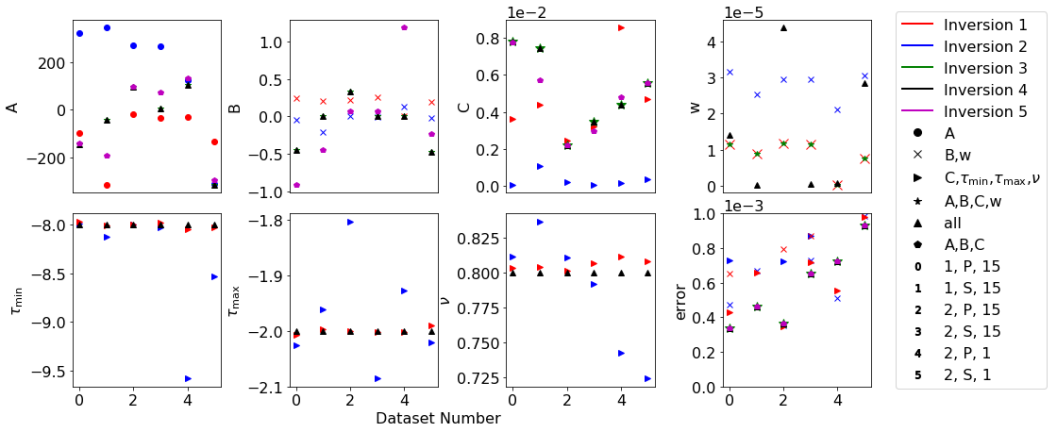

Figure 12. This figure compares the recovered parameters for the four different inversions run on the data. The parameters for the various inversions are shown in Table 2. The color indicates the inversion number and different symbols are used to indicate which parameters are fit in the inversion. Note that the green and black symbols are often on top of one another and that the green symbols overlap with the red for w. For the error plot, we have cut-off the errors when fitting only A (inversions 1A and 2A) as these are roughly ten times those of the other inversions (see Table 2). The legend values for the dataset number (x-axis) give the sample number, probe type and applied load.

Table 2. Input parameters and L_2-data misfit for each of the four inversion strategies tested. Setting $B = 1B$ as the initial parameters indicates that the value of B is fixed to the recovered value from Inversion 1B. The errors reported are for Sample 1, with a P-probe at 15 MPa; errors for other inversions are similar as can be seen in Figure 12(h). For inversion 4, initial values are either the results of inversion 3 or the same as their settings in inversion 3.

Inversion	parameters fit	other parameter settings	initial values	$\|\text{misfit}\|_2$
1A	A	B=C=0	20.	2.5e-3
1B	B,w	A=C=0	(0.4,1.5e-6)	6.5e-4
1C	C,$\tau_{\min}, \tau_{\max}, \nu$	A=B=0	(0.01,-8,-2,0.8)	4.3e-4
2A	A	results of 1B,1C	results of 1A	2.4e-3
2B	B,w	results of 1A,1C	results of 1B	4.7e-4
2C	C,$\tau_{\min}, \tau_{\max}, \nu$	results of 1B,1C	results of 1C	7.3e-4
3	A,B,C,w	($\tau_{\min}, \tau_{\max}, \nu$)=(-8,-2,0.8)	(20,0.4,0.01,1.5e-6)	3.4e-4
4	all	–	results of 3	3.4e-4
5	A,B,C	(w,$\tau_{\min}, \tau_{\max}, \nu$)=(2e-5,-8,-2,0.8)	(-140,-0.4,0.01)	3.4e-4

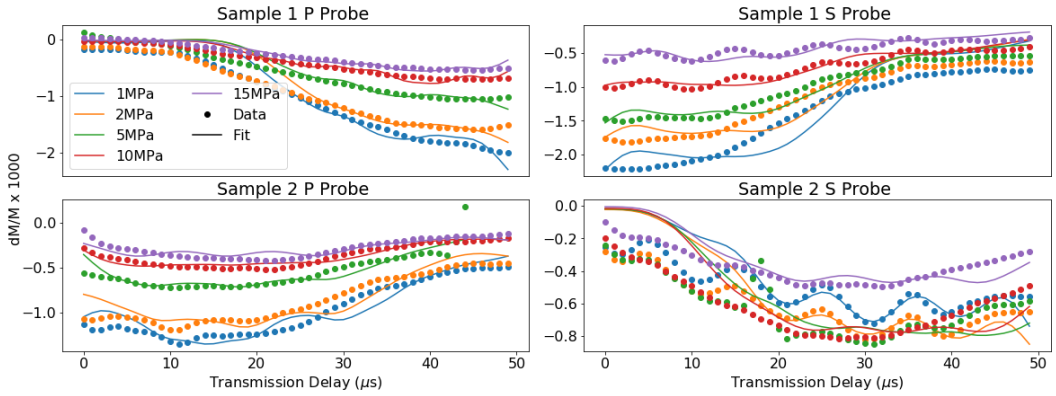

Figure 13. The data fits, using inversion strategy 3 for all of the datasets collected, and the residuals (bottom). Overall the model fits the data, though better for decreasing amplitudes of dM/M than for increasing. Note that the y-axis values are scaled by 1000 for ease of plotting.

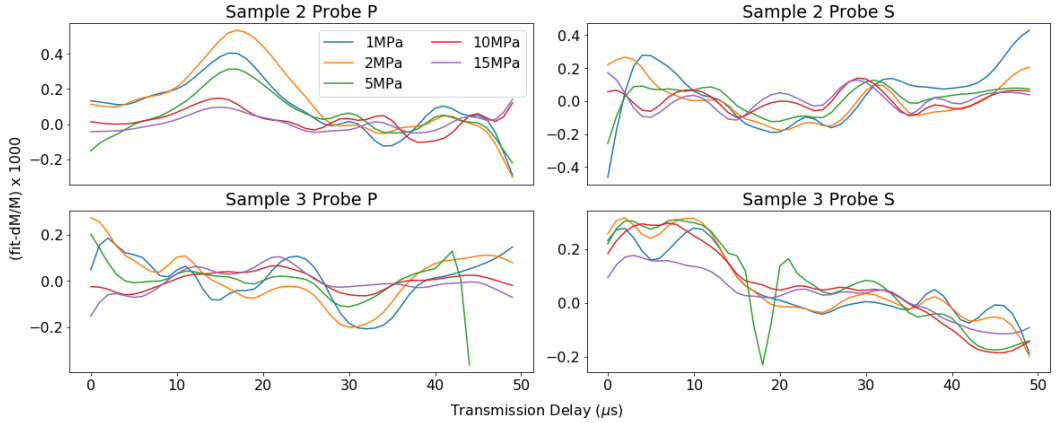

Figure 14. The data residuals, using inversion strategy 3 for all of the datasets collected. Overall the residuals are small, but there are clear trends, particularly for Sample 3 and an S probe. Note that the y-axis values are scaled by 1000 for ease of plotting.

2 with the S-probe there is a definite decreasing trend to the residuals. This is probably part of the same problem that we see in that the model has trouble fitting this dataset at smaller transmission delays.

Figure 15 shows how the model parameters evolve with applied load. When looking at the results of inversion 3, we see that there (left two columns) may be some tradeoff between B and w, as mentioned above. To mitigate this, we fix $w = 2 \times 10^{-5}$ and recompute A, B, C for all datasets. This does not significantly change either the data fit or the values of A, so we plot only the values of B and C in the rightmost column.

The clearest trend is in C, which decreases monotonically with load for all samples. This indicates that we are indeed closing connections in all samples as we increase the load. There is no clear trend in B, when fitting both B and w, although we do see a clear decrease in B with applied stress when we fix w (right column). This variability indicates that we may not be effecting the strength of the shear mechanism as consistently as the connection mechanism. That said, given that in inversions 1 and 2 we found that either B or C could explain our data, it is plausible that there are trade-offs between B and C that are not captured in this inversion. Although not quite as uniform, there is also a decrease in A with applied load so the strain-dependence of the signal also decreases with applied load. Interestingly this decrease seems to occur almost entirely before 5 MPa indicating that this mechanism is effective only at relatively low applied loads.

Although it is more difficult to interpret differences between the samples and probe-types, we nonetheless note a few trends. First, C is larger for Sample 2 than sample 1 whereas B is positive for Sample 1 and negative for Sample 2. The P-probe has significantly smaller $|B|$ in both samples, whereas both probes have similar values for C. This is because while in both cases the applied strain (from the pump) is roughly the same, we sense that strain in different ways: once with a change in P-wave modulus (P-probe, sensing $\kappa + 2/3\mu$), and once with a change in shear modulus (S-probe, sensing μ). It gives us some confidence in our data and model fitting that we see that the shear modulus is more sensitive to changes in the shearing mechanism whereas both moduli are sensitive to changes in the connections across the cracks. When looking at the C-values, Sample 2 has significantly larger C values than Sample 1, despite Sample 1 having a larger absolute change in modulus. The larger change in modulus seems to be accounted for by generally larger A values in Sample 1 than in Sample 2 as well as by the difference in sign in B. We would expect the strain applied by the pump (which is ϵ_{12}) to have a larger impact on Sample 1 where the normals to the crack faces align with the particle motion of the wave, explaining the larger A-value. That the change in C is larger in Sample 2 is likely because the normals to the cracks are aligned with the direction of the applied load so we would expect larger changes in across-crack connections in Sample 2 than in Sample 1.

To end this section we comment on the robustness of our observations. That C decreases nearly montonically with applied load is robust, as is the fact that C is larger for Sample 2 than for Sample 1. We see this pattern in all of our inversions, regardless

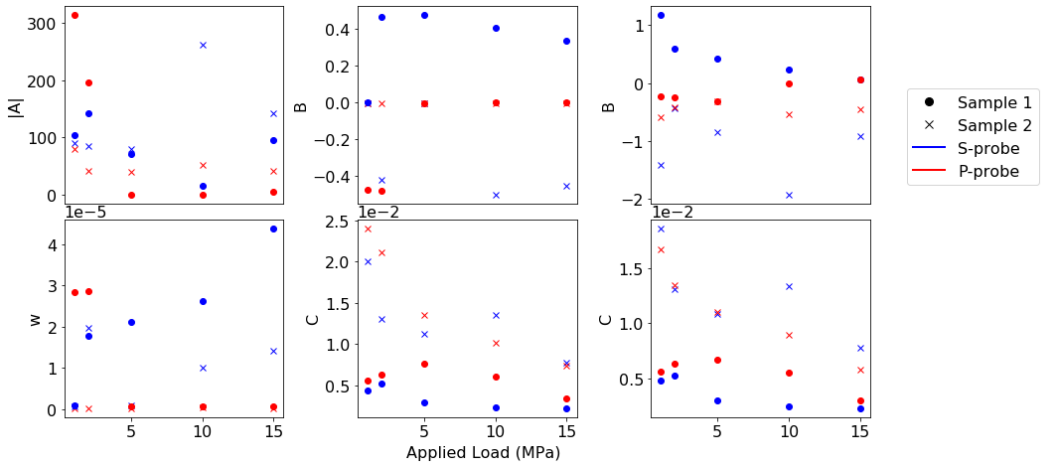

Figure 15. Fit parameters as a function of pressure. We show only A, B, C, w because $\tau_{\min}, \tau_{\max}, \nu$ did not update significantly over the inversions and do not show any trend as a function of applied load. The panels on the right show the results of inverting for only A, B, C, with $w = 2 \times 10^{-5}$ fixed.

of starting parameters or bounds on allowable parameter values. The trends in A and B are less robust. For example, there is reason to restrict, $A, B, C > 0$, as this implies that increasing strain increases the change in modulus in all cases, and that those changes are in phase with the applied strain. If we do this, the trend in B changes significantly, but notably the data fit also deteriorates and we are not able to fit some of the oscillations we see particularly in the Sample 3 S-probe data, as shown in Figure 16. Because of this, we choose to interpret the results allowing for negative values of A, B, C (though we only ever recover negative values of A and B).

7 Discussion

What is clear about our data is that the delays diminish with applied load. This is a clear indication that the nonlinearity is influenced by the sorts of small-scale cracks and other features whose properties depend strongly on the applied stress. This is as expected; it is well known that cracks are a driver of nonlinearity (Guyer & Johnson, 1999, 2009). What is interesting about these data is that other indicators of closing and aligned cracks seem to be largely negative, while the nonlinearity is quite clearly dependent on the applied stress, the relative orientation of the pump and the layering of the sample, and on the wave polarization. We see a weakening of the nonlinear effect over relatively

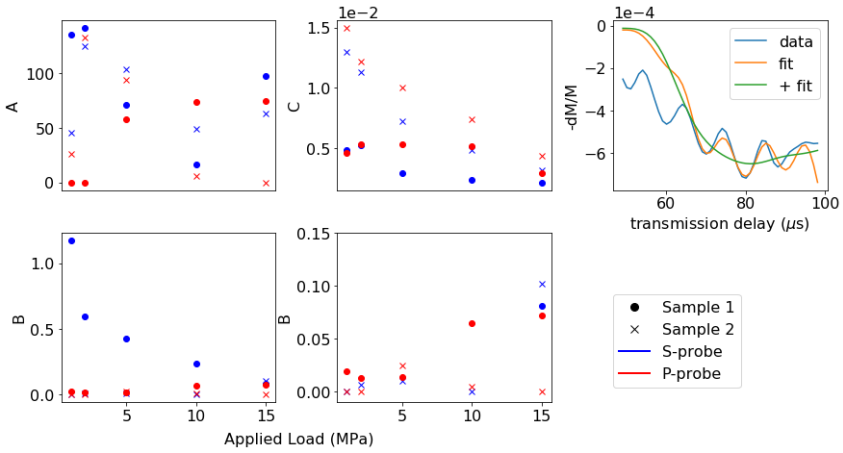

Figure 16. Re-fitting the dataset keeping $(A, B, C) > 0$ changes the response of A and B with applied load, and also worsens the quality of datafit. In the legend "+fit" is the datafit with the A, B, C parameters shown here, and "fit" uses those from inversion 4. The dataset shown is from Sample 3, 1 MPa and an S-probe. The middle bottom panel shows a zoom of the recovered B values.

small applied loads, in agreement with works that show weakening in the nonlinear signal at 10 MPa (e.g. Zinszner et al. (1997); Riviére et al. (2016)). We do not think that we have applied enough stress to produce new cracks as this seems to occur closer to 40 MPa (e.g. Browning et al. (2017)). We have to be careful mixing the effects of confining pressure studied by others with those of uniaxial stress studied here. In Rusmanugroho et al. (2020), they show that a simple 5-constant nonlinear model coupled with an effective medium theory to model cracks is able to reproduce the observed dependence of the nonlinear response on the relative orientation of the pump/probe system and the layering in the sample. (That work assumes cracks aligned with the layering.) That result is consistent with what we report here in that the nonlinear signal diminishes with applied load and consequently decreasing crack density.

Rivière et al. (2015) show that they have two clear mechanisms, as is also discussed by Scalerandi et al. (2015), where they divide these mechanisms into clapping and hysteresis (there is not firm indication that these are the same two mechanisms found by Rivière et al.). Our results seems to agree with the presence of two mechanisms. The first mechanism, characterized by the signal at the frequency of the pump seems independent of the applied load (Figure 3), as well as the pump driving voltage (Figure 4)

and crack orientation (TenCate et al., 2016). The second mechanism, which follows the shape of the envelope of the pump signal depends strongly on load as well as both pump driving amplitude and crack orientation. In addition, in Figure 15, we see that the number of broken connections predicted by the SSL model decreases with applied load. This makes sense as applying the load should close fractures, thus increasing the number of closed connections. We also see a decrease in the measure of shear motion on the cracks (B) from the SSL model, both diminishing with applied load and being distinctly smaller when we measure the change in shear-modulus vs P-wave modulus. This is all consistent with the closing of some connections, while still allowing those connections to slide and the rock to respond directly to an applied strain. We perhaps see some agreement with the idea of Zhao, Qiu, Jacobs, and Qu (2016) that some applied load may be needed on crack faces to allow them to be close enough to slide against one another in that we see some increase in B for some datasets at low loads. Confirming this would require more data at lower loads. The fact that we retain the signal at the pump frequency over the full range of applied load is an indication that it is this signal that we would expect to see in deeper rocks. Although it is tempting to conclude that this signal is only from shearing on cracks (i.e. the B part of the model), we should not discount the strain mechanism governed by A. Although trends in A are not as clear as those for B and C, this signal is also at the frequency of the applied strain (or twice it) and does definitely show some decay with applied load. The fact that we get the most robust changes in C is consistent with observations by Sens-Schönfelder et al. (2018) that it is the friction mechanism that controls many of the standard nonlinear mechanisms.

Another result of interest is that we do not see a signal at the frequency of the strain rate. For a pump of 90 kHz, the nyquist sampling rate for $|\dot{\epsilon}|$ is 2.78 μs, which is well above our sampling of 1 μs, so we do not think that this is the result of undersampling in that variable. It is clear, however that we do not see a dependence on strain-rate and that we get a much better fit to the SSL model if we low-pass filter the strain-rate. The precise reason for this is somewhat unclear. It could be that the strain mechanism is simply small and that it is dwarfed by other signals. But we do see, at least in some of the data, a consistent signal at the pump frequency, which we would expect to be proportional to strain that is not included in other models nor seen in other data to our knowledge. This is hinted at by Sens-Schönfelder and Eulenfeld (2019) when discussing mismatches between their model and that of Riviére et al. (2016).

It is somewhat counter-intuitive that we do not see a difference in the data trend for the two samples despite the different relative orientation of the bedding planes and the applied load. Batzle et al. (1980) see distinct opening of vertical cracks at the sort of loads we are applying, albeit in much smaller samples, which would lead us to expect that we would open vertical cracks. The alignment that results in the anisotropy in our samples is perhaps generated by aligned structures that are too small to be visualized with an SEM and as a result of their size they perhaps go from steady state to open to flattened over even the small range of applied stress used here. Another potential explanation is that our results are not sensitive to cracks as visualized in an SEM, but are instead sensitive to some other structures connecting the layers of the samples.

The role of fluids in nonlinearity is a subject of recent interest, and these data are not meant to enter into that discussion. The applied loads here are not large enough to limit pore-scale flow (Gist (1994) find that 40 MPa is sufficient to limit some pore-scale flow), and so we cannot rule out the movement of water as a significant mechanism in our results. Such movement is shown to happen during NRUS by Bittner and Popovics (2019).

We chose to compare our data only to the SSL model because it is straighforward to implement and accounts for several different mechanisms explicitly and separately. Aspects of our data could certainly also be compared explicitly with the extension of PM-space proposed by Scalerandi et al. (2015) or the bi-linear stiffness model proposed by Zhao, Qiu, Jacobs, and Qu (2016). We could also explicitly model the experiment as done by Pecorari (2015) and Rusmanugroho et al. (2020), but incorporating a uniaxial static load into those experiments would be challenging. We do not account for dissipation of any kind in our interpretations of our data. Investigating the effects of dissipation and in particular on the dissipative nonlinearity may lead to better agreement between models and our data (Broda et al., 2014).

To end this section, we return to our original question of how these results impact the observations of seismic velocity change and recovery after large earthquakes. Given our observations that the lower-frequency part of our signal (at the scale of the pump envelope) is the part of the signal that decays with applied load, it would seem logical to conclude that most of the signals responsible for the field-scale observations are the result of relaxation processes in the near-surface where the loads are small enough for

these larger-scale signals to exist. This is consistent with the results of (Hobiger et al., 2016) who find increasing velocity changes with frequency indicating that the strongest signals come from shallower depths. This of course assumes that these effects are due to the same inter-grain connections at both scales.

8 Conclusions

We present a dataset showing the evolution of the nonlinear interaction of different wave-types as a function of applied uniaxial load. We carefully examine our samples and determine that they do not have aligned structures at the scale of an SEM image, despite the fact that we see clear velocity anisotropy and layering. We measure how the velocity of our samples change with applied load, and use this to conclude that most of the cracks in both samples are closing as we apply the load. We then fit our data to a recently proposed model and use this model to analyze which mechanisms are active in controlling the signals that we see. We find that we have a balance between a strain, crack sliding, and connection mechanism and that all three mechanisms decrease with applied load. We find that using an S-wave probe to measure changes in the shear-modulus is more sensitive to the shearing mechanism and that only the connection mechanism seems to depend strongly on the orientation of the layering and thus microstructures of the samples. Our work supports two mechanisms controlling the nonlinearity as seen by others, and also that many signals recovered from earthquake data are likely coming from the near-surface. Our data also support the idea that nonlinear measurements are more sensitive to aligned structures and changes in these structures than the linear techniques used to characterize the sample.

Acknowledgments

This work is supported by Chevron and with grants from the Natural Sciences and Engineering Research Council of Canada (NSERC) Industrial Research Chair Program and InnovateNL. Funding is also acknowledeged from NSERC's Discovery Grant program. Computational support from ComputeCanada and ACENET is gratefully acknowledged. Data are available via the Harvard Dataverse at: `https://doi.org/10.7910/DVN/QRUZ9S`.

References

Alkhalifah, T., & Tsvankin, I. (1995). Velocity analysis for transversely isotropic me-

dia. *Geophysics*, *60*(5), 1550–1566.

Aoki, Y. (2015). Monitoring temporal changes of seismic properties. *Frontiers in Earth Science*, *3*, 42.

Arena, A., Delle Piane, C., & Sarout, J. (2014). A new computational approach to cracks quantification from 2D image analysis: Application to micro-cracks description in rocks. *Computers and Geosciences*, *66*(May), 106–120. doi: 10.1016/j.cageo.2014.01.007

Asaka, M., Luo, M., Yamatani, T., Kato, A., Yoshimatsu, K., & Knapp, L. (2018). 4D seismic feasibility study: The importance of anisotropy and hysteresis. *The Leading Edge*, *37*(9), 688-698. Retrieved from `https://doi.org/10.1190/tle37090688.1` doi: 10.1190/tle37090688.1

Batzle, M., Simmons, G., & Siegfried, W. (1980). Microcrack closure in rocks under stress: Direct observation. *Journal of Geophysical Research*, *85*, 7072–7090.

Benson, P., Meredith, P., Platzman, E., & White, R. (2005, oct). Pore fabric shape anisotropy in porous sandstones and its relation to elastic wave velocity and permeability anisotropy under hydrostatic pressure. *International Journal of Rock Mechanics and Mining Sciences*, *42*(7-8), 890–899. Retrieved from `http://linkinghub.elsevier.com/retrieve/pii/S1365160905000705` doi: 10.1016/j.ijrmms.2005.05.003

Bittner, J., & Popovics, J. S. (2019). Direct imaging of moisture effects during slow dynamic nonlinearity. *Applied Physics Letters*, *114*(2), 021901.

Boresi, A. P., & Schmidt, R. J. (2003). *Advanced mechanics of materials (6th edition)*. Hoboken, NJ: John Wiley & Sons.

Borri-Brunetto, M., Chiaia, B., & Ciavarella, M. (2001). Incipient sliding of rough surfaces in contact: a multiscale numerical analysis. *Computer methods in applied mechanics and engineering*, *190*(46-47), 6053–6073.

Bose, K., & Dorfmann, A. (2009). Computational aspects of a pseudo-elastic constitutive model for muscle properties in a soft-bodied arthropod. *International Journal of Non-Linear Mechanics*, *44*(1), 42–50.

Brenguier, F., Campillo, M., Hadziioannou, C., Shapiro, N. M., Nadeau, R. M., & Larose, E. (2008). Postseismic relaxation along the San Andreas fault at Parkfield from continuous seismological observations. *Science*, *321*(5895), 1478–1481.

Brenguier, F., Campillo, M., Takeda, T., Aoki, Y., Shapiro, N., Briand, X., ... Miyake, H. (2014). Mapping pressurized volcanic fluids from induced crustal seismic velocity drops. *Science*, *345*(6192), 80–82.

Broda, D., Staszewski, W., Martowicz, A., Uhl, T., & Silberschmidt, V. (2014). Modelling of nonlinear crack–wave interactions for damage detection based on ultrasound—a review. *Journal of Sound and Vibration*, *333*(4), 1097–1118.

Browning, J., Meredith, P. G., Stuart, C. E., Healy, D., Harland, S., & Mitchell, T. M. (2017). Acoustic characterization of crack damage evolution in sandstone deformed under conventional and true triaxial loading. *Journal of Geophysical Research: Solid Earth*, *122*(6), 4395–4412. doi: 10.1002/2016JB013646

Catheline, S., Wu, F., & Fink, M. (1999, May). A solution to diffraction biases in sonoelasticity: The acoustic impulse technique. *The Journal of the Acoustical Society of America*, *105*(5), 2941–50. Retrieved from `http://www.ncbi.nlm.nih.gov/pubmed/10335643`

Durand, S., Montagner, J., Roux, P., Brenguier, F., Nadeau, R., & Ricard, Y. (2011). Passive monitoring of anisotropy change associated with the Parkfield 2004 earthquake. *Geophysical Research Letters*, *38*(13).

Froment, B., Campillo, M., Chen, J., & Liu, Q. (2013). Deformation at depth associated with the 12 May 2008 Mw 7.9 Wenchuan earthquake from seismic ambient noise monitoring. *Geophysical Research Letters*, *40*(1), 78–82.

Gallot, T., Malcolm, A. E., Szabo, T. L., Brown, S., Burns, D., & Fehler, M. (2015). Characterizing the nonlinear interaction of S- and P-waves in a rock sample. *Journal of Applied Physics*, *117*, 034902.

Gassenmeier, M., Sens-Schönfelder, C., Eulenfeld, T., Bartsch, M., Victor, P., Tilmann, F., & Korn, M. (2016). Field observations of seismic velocity changes caused by shaking-induced damage and healing due to mesoscopic nonlinearity. *Geophysical Journal International*, *204*(3), 1490–1502.

Gholami, A. (2018). *Personal communication.* (Proposed the change from parabola to sinc function.)

Gist, G. (1994). Fluid effects on velocity and attenuation in sandstones. *The Journal of the Acoustical Society of America*, *96*(2), 1158–1173. Retrieved from `http://scitation.aip.org/content/asa/journal/jasa/96/2/10.1121/`

1.410389

Guéguen, Y., & Kachanov, M. (2012). Effective elastic properties of cracked rocks—an overview. *Mechanics of Crustal Rocks*, *533*, 73–125. Retrieved from http://link.springer.com/chapter/10.1007/978-3-7091-0939-7{_}3

Guyer, R. A., & Johnson, P. A. (1999). Nonlinear Mesoscopic Elasticity: Evidence for a New Class of Materials. *Physics Today*, *52*(4), 30. Retrieved from http://scitation.aip.org/content/aip/magazine/physicstoday/article/52/4/10.1063/1.882648 doi: 10.1063/1.882648

Guyer, R. A., & Johnson, P. A. (2009). *Nonlinear mesoscopic elasticity: The complex behaviour of rocks, soil, concrete*. John Wiley & Sons.

Hayes, L., & Malcolm, A. (2017). How fracture orientation and particle motion impact nonlinear interactions in an elastic medium. *2017 SEG Technical Program Expanded Abstracts*, 1–5.

Hayes, L., Malcolm, A., Moravej, K., & Butt, S. (2018). Nonlinear interactions of P and S waves under uniaxial stress. *POMA proceedings of the 21st International Symposium on Nonlinear Acoustics*.

Hillers, G., Husen, S., Obermann, A., Planès, T., Larose, E., & Campillo, M. (2015). Noise-based monitoring and imaging of aseismic transient deformation induced by the 2006 Basel reservoir stimulation. *Geophysics*, *80*(4), KS51–KS68.

Hobiger, M., Wegler, U., Shiomi, K., & Nakahara, H. (2012). Coseismic and post-seismic elastic wave velocity variations caused by the 2008 Iwate-Miyagi Nairiku earthquake, Japan. *Journal of Geophysical Research: Solid Earth*, *117*(B9).

Hobiger, M., Wegler, U., Shiomi, K., & Nakahara, H. (2016). Coseismic and post-seismic velocity changes detected by passive image interferometry: comparison of one great and five strong earthquakes in Japan. *Geophysical Journal International*, *205*(2), 1053–1073.

Hughes, D., & Kelly, J. (1953). Second-order elastic deformation of solids. *Physical Review*, *89*(1940). Retrieved from http://adsabs.harvard.edu/abs/1953PhRv...92.1145H

Landau, L., & Lifshitz, E. (1970). *Theory of elasticity*. Pergamon Press.

Lebedev, A., & Ostrovsky, L. (2014). A unified model of hysteresis and long-time relaxation in heterogeneous materials. *Acoustical Physics*, *60*(5), 555–561.

765 Li, X., Sens-Schönfelder, C., & Snieder, R. (2018). Nonlinear elasticity in resonance
766 experiments. *Physical Review B*, *97*(14), 144301.

767 Lott, M., Payan, C., Garnier, V., Vu, Q. A., Eiras, J. N., Remillieux, M. C., ... Ul-
768 rich, T. (2016). Three-dimensional treatment of nonequilibrium dynamics and
769 higher order elasticity. *Applied Physics Letters*, *108*(14), 141907.

770 Lott, M., Remillieux, M. C., Bas, P.-y. L., Ulrich, T. J., Garnier, V., & Payan, C.
771 (2016). From local to global measurements of nonclassical nonlinear elas-
772 tic effects in geomaterials. *Journal of the Acoustical Society of America*,
773 *140*(EL231). Retrieved from `http://dx.doi.org/10.1121/1.4962373` doi:
774 10.1121/1.4962373

775 Lott, M., Remillieux, M. C., Garnier, V., Le Bas, P.-Y., Ulrich, T. J., & Payan, C.
776 (2017). Nonlinear elasticity in rocks: A comprehensive three-dimensional
777 description. *Physical Review Materials*, *1*(2), 023603. Retrieved from
778 `http://link.aps.org/doi/10.1103/PhysRevMaterials.1.023603` doi:
779 10.1103/PhysRevMaterials.1.023603

780 McCall, K. (1994). Theoretical study of nonlinear elastic wave propagation. *Journal*
781 *of Geophysical Research: Solid Earth*, *99*, 2591–2600. Retrieved from `http://`
782 `onlinelibrary.wiley.com/doi/10.1029/93JB02974/full`

783 McCall, K., & Guyer, R. (1994). Equation of state and wave propagation in hys-
784 teretic nonlinear elastic materials. *Journal of Geophysical Research: Solid*
785 *Earth*, *99*(94). Retrieved from `http://onlinelibrary.wiley.com/doi/`
786 `10.1029/94JB01941/full`

787 Nazarov, V. E., Sutin, A. M., Nazarov, V. E., & Sutin, A. M. (1997). Nonlinear
788 elastic constants of solids with cracks. *The Journal of the Acoustical Society of*
789 *America*, *102*, 3349. doi: 10.1121/1.419577

790 Nishimura, T., Uchida, N., Sato, H., Ohtake, M., Tanaka, S., & Hamaguchi, H.
791 (2000). Temporal changes of the crustal structure associated with the M6. 1
792 earthquake on September 3, 1998, and the volcanic activity of Mount Iwate,
793 Japan. *Geophysical Research Letters*, *27*(2), 269–272.

794 Norris, A. (2007). Small-on-large theory with applications to granular materials and
795 fluid/solid systems. In *Waves in nonlinear pre-stressed materials* (pp. 27–62).
796 Springer.

797 Nye, J. F., et al. (1985). *Physical properties of crystals: their representation by ten-*

sors and matrices. New York: Oxford university press.

Obermann, A., Froment, B., Campillo, M., Larose, E., Planes, T., Valette, B., ... Liu, Q. (2014). Seismic noise correlations to image structural and mechanical changes associated with the Mw 7.9 2008 Wenchuan earthquake. *Journal of Geophysical Research: Solid Earth*, *119*(4), 3155–3168.

Obermann, A., Planès, T., Larose, E., & Campillo, M. (2019). 4-D imaging of subsurface changes with coda waves: Numerical studies of 3-d combined sensitivity kernels and applications to the $M_$w 7.9, 2008 Wenchuan earthquake. *Pure and Applied Geophysics*, *176*(3), 1243–1254.

Obermann, A., Planès, T., Larose, E., Sens-Schönfelder, C., & Campillo, M. (2013). Depth sensitivity of seismic coda waves to velocity perturbations in an elastic heterogeneous medium. *Geophysical Journal International*, *194*(1), 372–382.

Ostrovsky, L., & Johnson, P. (2001). Dynamic nonlinear elasticity in geomaterials. *Rivista del nuovo cimento*, *24*(7). Retrieved from `http://lanl.gov/orgs/ees/ees11/geophysics/nonlinear/2001/LaRivista.pdf`

Pecorari, C. (2015, jan). Modeling the elasto-acoustic hysteretic nonlinearity of dry Berea sandstone. *Wave Motion*, *52*, 66–80. Retrieved from `http://linkinghub.elsevier.com/retrieve/pii/S0165212514001140` doi: 10.1016/j.wavemoti.2014.09.001

Poupinet, G., Ellsworth, W., & Frechet, J. (1984). Monitoring velocity variations in the crust using earthquake doublets: An application to the Calaveras Fault, California. *Journal of Geophysical Research: Solid Earth*, *89*(B7), 5719–5731.

Remillieux, M. C., Ulrich, T. J., Goodman, H. E., & Ten Cate, J. A. (2017). Propagation of a Finite-Amplitude Elastic Pulse in a Bar of Berea Sandstone: A Detailed Look at the Mechanisms of Classical Nonlinearity, Hysteresis, and Nonequilibrium Dynamics. *Journal of Geophysical Research: Solid Earth*, *122*(11), 8892–8909. doi: 10.1002/2017JB014258

Renaud, G., Calle, S., Remenieras, J. P., & Defontaine, M. (2008, July). Exploration of trabecular bone nonlinear elasticity using time-of-flight modulation. *IEEE transactions on ultrasonics, ferroelectrics, and frequency control*, *55*(7), 1497–507. Retrieved from `http://www.ncbi.nlm.nih.gov/pubmed/18986939` doi: 10.1109/TUFFC.2008.825

Renaud, G., Le Bas, P.-Y., & Johnson, P. A. (2012, June). Revealing highly

complex elastic nonlinear (anelastic) behavior of Earth materials applying a new probe: Dynamic acoustoelastic testing. *Journal of Geophysical Research*, *117*(B6), B06202. Retrieved from http://doi.wiley.com/10.1029/2011JB009127 doi: 10.1029/2011JB009127

Renaud, G., Talmant, M., Callé, S., Defontaine, M., & Laugier, P. (2011, December). Nonlinear elastodynamics in micro-inhomogeneous solids observed by head-wave based dynamic acoustoelastic testing. *The Journal of the Acoustical Society of America*, *130*(6), 3583–9. Retrieved from http://www.ncbi.nlm.nih.gov/pubmed/22225015 doi: 10.1121/1.3652871

Riviére, J., Pimienta, L., Scuderi, M., Candela, T., Shokouhi, P., Fortin, J., ... Johnson, P. A. (2016). Frequency, pressure, and strain dependence of nonlinear elasticity in Berea Sandstone. *Geophysical Research Letters*, *43*(7), 3226–3236.

Rivière, J., Renaud, G., Guyer, R. A., & Johnson, P. A. (2013). Pump and probe waves in dynamic acousto-elasticity: Comprehensive description and comparison with nonlinear elastic theories. *Journal of Applied Physics*, *054905*, 1–19. Retrieved from http://scitation.aip.org/content/aip/journal/jap/114/5/10.1063/1.4816395

Rivière, J., Shokouhi, P., Guyer, R. A., & Johnson, P. A. (2015). A set of measures for the systematic classification of the nonlinear elastic behavior of disparate rocks. *Journal of Geophysical Research: Solid Earth*, *120*(3), 1587–1604.

Rubinstein, J. L., Uchida, N., & Beroza, G. C. (2007). Seismic velocity reductions caused by the 2003 Tokachi-Oki earthquake. *Journal of Geophysical Research: Solid Earth*, *112*(B5).

Rusmanugroho, H., Darijani, M., & Malcolm, A. (2020). A numerical model for the nonlinear interaction of elastic waves with cracks. *Wave Motion*, *92*, 102444. doi: https://doi.org/10.1016/j.wavemoti.2019.102444

Sánchez-Pastor, P., Obermann, A., Schimmel, M., Weemstra, C., Verdel, A., & Jousset, P. (2019). Short-and long-term variations in the reykjanes geothermal reservoir from seismic noise interferometry. *Geophysical Research Letters*.

Sato, H. (1988). Temporal change in scattering and attenuation associated with the earthquake occurrence—a review of recent studies on coda waves. *Pure and Applied Geophysics*, *126*(2-4), 465–497.

Sayers, C., & Kachanov, M. (1995). Microcrack-induced elastic wave anisotropy of brittle rock. *Journal of Geophysical Research: ...*, *100*(B3), 4149–4156. Retrieved from `http://onlinelibrary.wiley.com/doi/10.1029/94JB03134/full`

Scalerandi, M., Idjimarene, S., Bentahar, M., & El Guerjouma, R. (2015). Evidence of microstructure evolution in solid elastic media based on a power law analysis. *Communications in Nonlinear Science and Numerical Simulation*, *22*(1-3), 334–347.

Sens-Schönfelder, C., & Eulenfeld, T. (2019). Probing the in situ elastic nonlinearity of rocks with earth tides and seismic noise. *Physical review letters*, *122*(13), 138501.

Sens-Schönfelder, C., Snieder, R., & Li, X. (2018). A model for nonlinear elasticity in rocks based on friction of internal interfaces and contact aging. *Geophysical Journal International*, *216*(1), 319–331.

Sens-Schönfelder, C., & Wegler, U. (2006). Passive image interferometry and seasonal variations of seismic velocities at merapi volcano, indonesia. *Geophysical research letters*, *33*(21).

Sens-Schönfelder, C., & Wegler, U. (2011). Passive image interferometry for monitoring crustal changes with ambient seismic noise. *Comptes Rendus Geoscience*, *343*(8-9), 639–651.

Snieder, R., Sens-Schönfelder, C., & Wu, R. (2016). The time dependence of rock healing as a universal relaxation process, a tutorial. *Geophysical Journal International*, *208*(1), 1–9.

Solodov, I. Y., Krohn, N., & Busse, G. (2002). CAN : an example of nonclassical acoustic nonlinearity in solids. *The Journal of the Acoustical Society of America*, *40*, 621–625.

Ten Cate, J., & Shankland, T. (1996). Slow dynamics in the nonlinear elastic response of Berea sandstone. *Geophysical Research Letters*, *23*(21), 3019–3022. Retrieved from `http://onlinelibrary.wiley.com/doi/10.1029/96GL02884/full`

TenCate, J. A., Malcolm, A. E., Feng, X., & Fehler, M. C. (2016). The effect of crack orientation on the nonlinear interaction of a P wave with an S wave. *Geophysical Research Letters*, *43*(12), 6146-6152. Retrieved from `https://`

agupubs.onlinelibrary.wiley.com/doi/abs/10.1002/2016GL069219 doi: 10.1002/2016GL069219

Tremblay, N., Larose, E., & Rossetto, V. (2010). Probing slow dynamics of consolidated granular multicomposite materials by diffuse acoustic wave spectroscopy. *The Journal of the Acoustical Society of America*, *127*(3), 1239–1243.

Tsvankin, I. (2012). *Seismic signatures and analysis of reflection data in anisotropic media*. Society of Exploration Geophysicists.

Vakhnenko, O. O., Vakhnenko, V. O., Shankland, T. J., & TenCate, J. A. (2006). Soft-ratchet modeling of slow dynamics in the nonlinear resonant response of sedimentary rocks. In *Aip conference proceedings* (Vol. 838, pp. 120–123).

Wang, Q.-Y., Campillo, M., Brenguier, F., Lecointre, A., Takeda, T., & Hashima, A. (2019). Evidence of changes of seismic properties in the entire crust beneath Japan after the Mw 9.0, 2011 Tohoku-Oki earthquake. *Journal of Geophysical Research: Solid Earth*.

Wegler, U., & Sens-Schönfelder, C. (2007, 03). Fault zone monitoring with passive image interferometry. *Geophysical Journal International*, *168*(3), 1029-1033. doi: 10.1111/j.1365-246X.2006.03284.x

Zaitsev, V., Gusev, V., Tournat, V., & Richard, P. (2014). Slow relaxation and aging phenomena at the nanoscale in granular materials. *Physical review letters*, *112*(10), 108302.

Zhao, Y., Qiu, Y., & Jacobs, L. J. (2016). Frequency-dependent tensile and compressive effective moduli of elastic solids with distributed penny-shaped microcracks. *Acta Mech*, *227*, 399–419. doi: 10.1007/s00707-015-1450-z

Zhao, Y., Qiu, Y., Jacobs, L. J., & Qu, J. (2016). A Micromechanics Model for the Acoustic Nonlinearity Parameter in Solids with Distributed Microcracks. *AIP Conference Proceedings*, *1706*(February 2016), 060001. doi: 10.1063/1.4940507

Zinszner, B., Johnson, P., & Rasolofosaon, P. (1997). Influence of change in physical state on elastic nonlinear response in rock: Significance of effective pressure and water saturation. *Journal of Geophysical Research*, *102*(96), 8105–8120. Retrieved from http://onlinelibrary.wiley.com/doi/10.1029/96JB03225/full